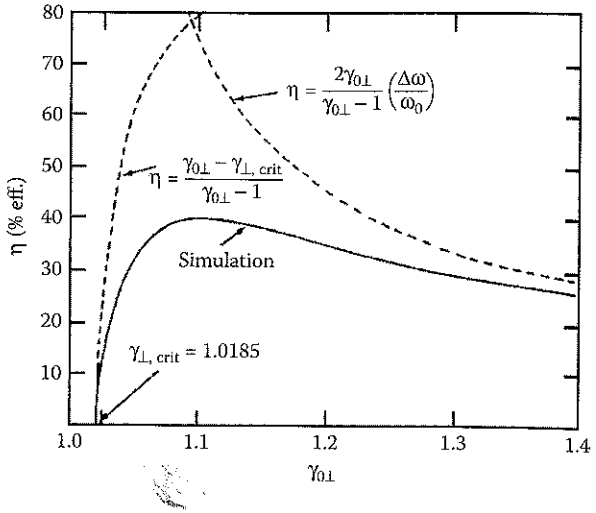

FIGURE 10.24
Calculated efficiency of a gyrotron in a frame of reference moving with the axial beam velocity in which $v_z = 0$. The analytical estimate shown in the dashed line to the left is based on rotational energy depletion as the saturation mechanism, while the estimate to the right assumes that phase trapping is the sole saturation mechanism. (From Sprangle, P. and Drobot, A.T., *IEEE Trans. Microwave Theory Tech.*, MTT-25, 528, 1977. With permission.)

trons to microwaves, η_e. The electronic efficiency is computed from $\eta_\perp$ by making a Lorentz transformation back to the laboratory frame of reference:[68]

$$\eta_e = \frac{\gamma_0\left(\gamma_{0\perp}-1\right)}{\gamma_{0\perp}\left(\gamma_0-1\right)}\eta_\perp \tag{10.19}$$

where $\gamma_0 = (1-\beta_{0\perp}^2-\beta_{0z}^2)^{-1/2}$. For a weakly relativistic beam (i.e., much less than 500 keV per electron), Equation 10.19 can be approximated by

$$\eta_e \approx \frac{\beta_{0\perp}^2}{\beta_{0\perp}^2+\beta_{0z}^2}\eta_\perp = \frac{\alpha^2}{1+\alpha^2}\eta_\perp \tag{10.20}$$

with $\alpha = \beta_{0\perp}/\beta_{0z} = v_{0\perp}/v_{0z}$.

Two primary means of increasing the efficiency of these devices involve tapering either the radius of the cavity or the applied magnetic field in the axial direction.[86] In either case, the basic idea is to begin bunching the beam under less than optimal conditions for maximum energy extraction, and then to pass the bunched beam into a region where it can more effectively surrender its energy to the microwaves. In cavity tapering, the electric field profile in the cavity is tailored in such a way that the highest amplitudes are reached toward the downstream end, by which point the beam has become bunched. In magnetic tapering, the field near the entrance of the cavity is held below a value at which strong resonance can occur, so that bunching is not accompanied by significant energy extraction. Further into the cavity, though, the magnetic field is increased to the resonance value, so that higher-efficiency extraction is accomplished by the bunched beam.

Because of the very high internal power levels in modern gyrotrons, depressed collectors are now used quite frequently to raise efficiency and thus reduce power loss to the cavity and collector walls, as well as to reduce radiation generation.[58] Depressed collectors are placed downstream of the interaction cavity, where the spent electrons are collected and their remaining kinetic energy is converted back to electrical energy to be recycled in the system. Efficiencies of 50% are now regularly seen in megawatt-class gyrotrons using this component (see Problem 10).

10.3.3 Gyrotron Operational Features

In this section, we consider both megawatt-class long-pulse or continuous gyrotrons and the relativistic gyrotrons developed at the NRL.

10.3.3.1 High-Average-Power Gyrotrons

The pace of development for the former is impressive. Consider the development of gyrotrons in the U.S. at CPI in Palo Alto, CA, by comparing the parameters and performance of a 110-GHz gyrotron described in a 1996 paper[87] and a 140-GHz gyrotron described in 2004.[88] A schematic of the former is shown in Figure 10.25. The notable features there are operation in the $TE_{22,6,1}$ mode, with a peak thermal wall loading of about 0.8 kW/cm^2; an internal mode converter using the dimpled-wall or Denisov converter developed at the Institute of Applied Physics in Nizhny Novgorod, which has an efficiency of 95%, as opposed to the earlier Vlasov converter with an efficiency of about 80%; output windows of double-disc sapphire with coolant running between the two discs; and a passive beam collection system. With beam voltage and current of 86 kV and 37.6 A, and an output of 1.013 MW, the efficiency of this gyrotron was 31%. To compare, the 2004 gyrotron operated in the $TE_{28,7,1}$ mode with a peak thermal wall loading of 0.3 kW/cm^2 measured in tests at only 500 kW of output; a dimpled-wall converter capable of coupling out 99% of the tube output; output windows of edge-cooled CVD diamond; and a single-stage depressed collector to recover beam energy. At 80 kV and 40 A in the electron gun, and an output power expected to be 1 MW, the efficiency is actually a bit smaller, at about 31%; however, the depressed collector raises the overall system efficiency to almost 42%.

At FZK Karlsruhe, work on a 1.5-MW, 165-GHz tube is aimed at ultimately making it possible to produce a 2-MW, 170-GHz tube that was expected for ITER, the international tokamak.[82] The 165-GHz tube operates in the $TE_{31,17}$ mode, with a 90-kV, 50-A electron gun and a nominal output of 1.5 MW, for

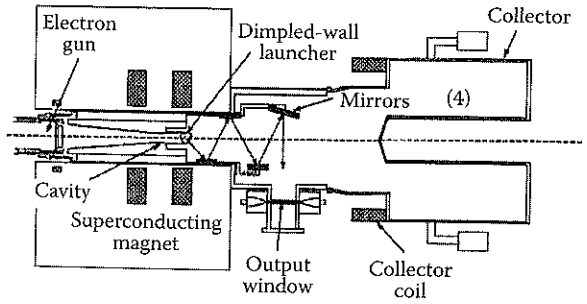

FIGURE 10.25
Schematic diagram of a 110-GHz gyrotron from CPI described in 1996. (From Felch, K. et al., *IEEE Trans. Plasma Sci.*, 24, 558, 1996. With permission.)

an efficiency of 33%; a depressed collector raises the system efficiency still higher, to 48%. This system uses a coaxial cavity.

10.3.3.2 Relativistic Gyrotrons

A series of papers dating to 1985 described high-peak-power experiments at 35 GHz with a relativistic gyrotron at the Naval Research Laboratory.[89–92] The most recent configuration of the experiment is shown in Figure 10.26. An electron beam is generated on an annular, explosive emission cathode on the VEBA pulse-line accelerator. Waveforms for the current and voltage from the accelerator are shown in Figure 10.27; the beam is emitted from the cathode at 1.2 MV and about 20 kA, but the apertured anode passes only about 2.5 kA. In this role, the anode also acts as an emittance filter. As it leaves the diode gap, the beam has very little $v_\perp$, so it is passed through a pump magnet coil, which imparts the perpendicular rotational mode motion to the electrons, as can be seen in the figure. Downstream, the gyrotron cavity is cylindrically symmetric, with a diameter of 3.2 cm and a calculated Q of 180 for the $TE_{6,2}$ mode, in the absence of the beam. Beyond, there is a 5° output taper transition to a drift tube 120 cm in length and 14 cm in diameter, followed by a 1-m output horn flaring to an output window 32 cm in diameter. Operating in this geometry, with a cavity field of 3.2 T, power levels of up to 250 MW at efficiencies as high as 14% have been achieved. The 40-nsec duration of the microwave pulse means that microwaves are produced for roughly the duration of the flat part of the VEBA voltage and current pulse.

The NRL experiments began in the mid-1980s. In the first set of experiments, a 350-kV, 800-A beam was emitted across a magnetic field from an explosive emission cathode to supply some initial transverse energy, and then the beam was adiabatically compressed by the field. At 8% efficiency 20 MW was generated, but the experiment lacked the necessary flexibility to improve that value markedly.[89] In a second version,[90,91] a higher-power beam, 900 kV and 1.6 kA, was generated in a foil-less diode and passed

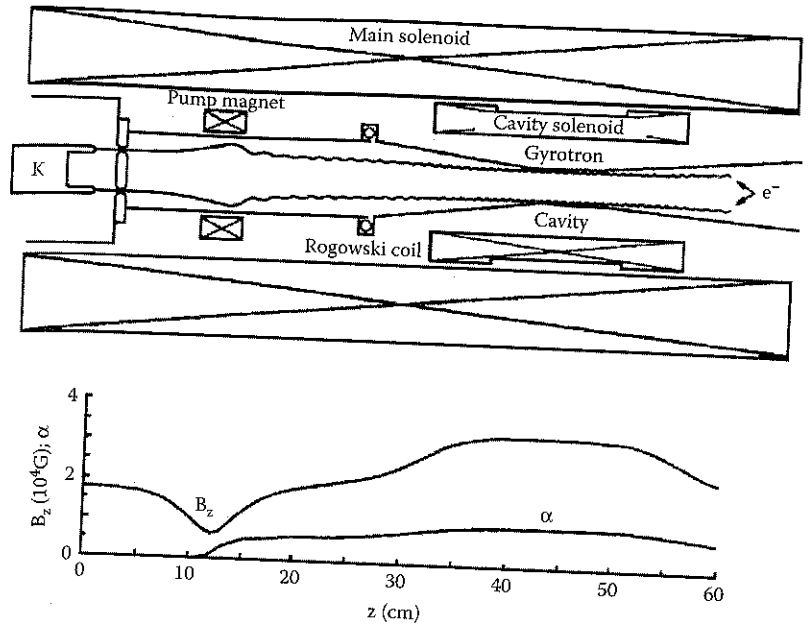

FIGURE 10.26
Configuration of the relativistic gyrotron experiments conducted on the VEBA pulse-line accelerator at NRL. (From Black, W.M. et al., *Phys. Fluids B*, 2, 193, 1990. With permission.)

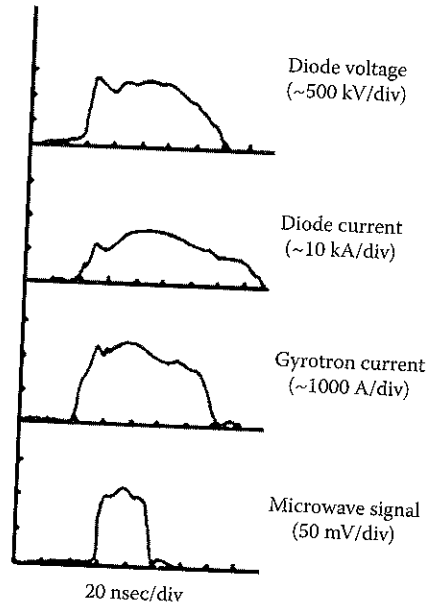

FIGURE 10.27
Accelerator and beam voltage and current waveforms from the experiment of Figure 10.26. (From Black, W.M. et al., *Phys. Fluids B*, 2, 193, 1990. With permission.)

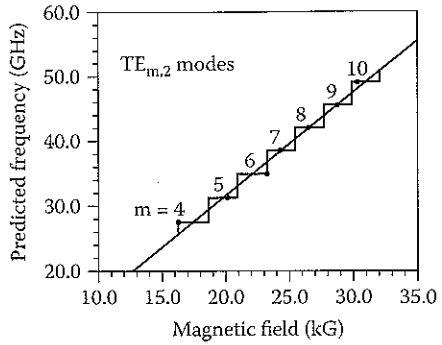

FIGURE 10.28
Step tuning of the NRL relativistic gyrotron through the TE_{m2} whispering-gallery modes by varying the cavity magnetic field. Points are experimental data, the straight line is a best fit to the data, and the "stair step" shows ranges of the magnetic field over which each mode is calculated to start for the beam current used. (From Gold, S.H. et al., *Phys. Fluids*, 30, 2226, 1987. With permission.)

through a magnetic wiggler to pump up $v_\perp$, which was then further increased by magnetic compression. This version produced 100 MW at 8% efficiency in a TE_{62} mode. Further, the gyrotron was shown to be step tunable through the whispering-gallery modes TE_{n2}, with n = 4 to 10, by varying the cavity magnetic field, as shown in Figure 10.28. Open-shutter photographs of the gas breakdown pattern in a low-pressure cell verified the field patterns associated with the expected modes. In this same experiment, 35 MW was produced in the TE_{13} cavity mode by cutting a slot on either side of the cavity to eliminate competition from the whispering-gallery modes. A shortcoming of this experiment was the rather low beam quality. Following those experiments, in experiments configured as shown in Figure 10.26, the group produced 250 MW at 14% efficiency.[92] An additional feature of those experiments was a set of computer simulations (using a single-cavity mode) designed to test the response of the gyrotron to the temporal voltage fluctuations of the electron beam (assuming that the current varied as the voltage $V^{3/2}$). Calculations of the microwave power envelopes for different magnetic fields and voltage waveforms with temporal variations that modeled the fluctuations seen in real experiments (i.e., without assuming a constant voltage during the pulse) showed varying sensitivities of the output to the voltage glitches of real waveforms, with different microwave power maxima for different portions of the voltage waveform — depending on the magnetic field — and complete interruptions of output power in response to certain voltage variations.

As a final point with regard to the issue of step tuning magnetrons, it is interesting to compare the rather clean behavior of the NRL gyrotron operating in relatively low order whispering-gallery modes to the situation for much higher order modes in a higher-frequency gyrotron at MIT.[93] The data for the latter are shown in Figure 10.29, plotted somewhat differently than

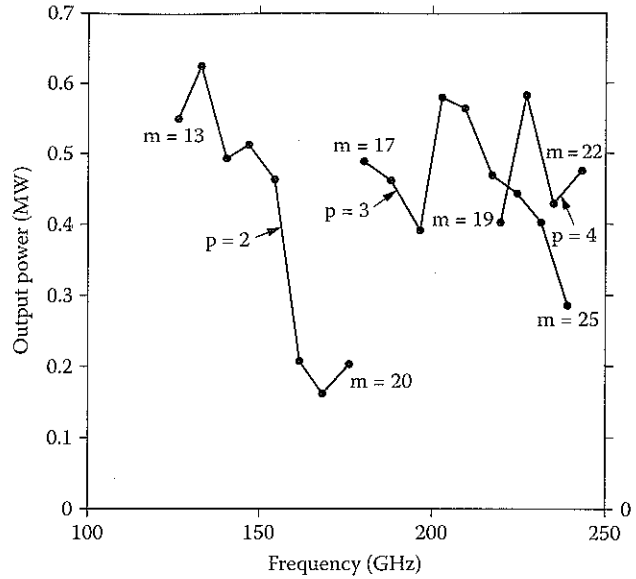

FIGURE 10.29
Peak output power measured at the frequencies shown by step tuning a gyrotron at MIT through the $TE_{m,p,1}$ modes. Operation in the different modes was achieved by varying the cavity magnetic field. (From Kreischer, K.E. and Temkin, R.J., *Phys. Rev. Lett.*, 59, 547, 1987. With permission.)

in Figure 10.28. Nevertheless, we see the complexity of step tuning TE_{mp} modes (remembering that m is the index on azimuthal field variations and p is the index on radial variations) by varying the magnetic field when m ranges as high as 25 for p = 2 to 4, with overlaps in frequency (albeit at different values of the magnetic field).

10.3.4 CARMs and Gyroklystrons

While gyrotrons are the most well known and studied ECMs, they are by no means the only variant of interest. Here we consider briefly two variants of interest from an HPM perspective: the CARM and the gyroklystron.

10.3.4.1 CARMs

Returning to Figure 10.22, we note that at sufficiently high electron energies, which implies large v_z, and resonant phase velocities, the ECM interaction leads to a CARM. The important conceptual feature of CARMs is autoresonance. To understand this concept, we consider the behavior of the cyclotron wave dispersion as the wave loses energy. Differentiating Equation 10.18 for s = 1, we determine the time rate of change of the resonant frequency as energy is drawn from the electrons into the microwave fields:

$$\frac{d\omega}{dt} = k_z \frac{dv_z}{dt} + \frac{d\omega_c}{dt} = k_z \frac{dv_z}{dt} - \omega_c \left(\frac{1}{\gamma} \frac{d\gamma}{dt} \right) \tag{10.21}$$

The derivatives of both $v_z = p_z/m\gamma$ and $\gamma = [1 + \mathbf{p}\bullet\mathbf{p}/(mc)^2]^{1/2}$ are determined from the equation of motion, from which we find

$$\frac{d\omega}{dt} = \frac{e\omega}{\gamma mc^2} v_\perp \bullet E_\perp \left[1 - \left(\frac{k_z c}{\omega} \right)^2 \right] \tag{10.22}$$

where $\mathbf{E}_\perp$ is the electric field component of a TE wave. Thus, $d\omega/dt$ vanishes as the phase velocity, ω/k_z, goes to the speed of light. In this event, as the electrons lose energy to the microwaves, the decrease in the term $k_z v_z$ is compensated by an increase in ω_c, with its inverse dependence on γ.[71,94,95] Alternatively, this effect is viewed as a cancellation of the effects of axial and azimuthal bunching (via the changes in v_z and γ, respectively). Thus, the electrons remain in resonance even as they surrender energy to the microwave fields. By contrast, note that in a gyrotron, $k_z \approx 0$, and the energy loss to azimuthal bunching is uncompensated. A calculation similar to that for FELs shows that in CARMs, the basic electron oscillation frequency, in this case ω_c, is strongly Doppler upshifted by an amount proportional to γ. Note, however, that since the cyclotron frequency is also proportional to γ^{-1}, the upshift in the CARM only scales as γ.

The CARM shown in Figure 10.30, an oscillator from the Institute of Applied Physics, was one of the first high power devices of this type.[62] To shorten the output wavelength from the 4.3 mm of early experiments using the lowest-order TE_{11} mode of the resonator, the CARM shown in the figure employed the TE_{41} mode to achieve a 2-mm output. The electron beam was generated with a pulse-line machine at a voltage of 500 to 600 kV and a current of about 1 kA. The system was immersed in a pulsed 2-T magnetic

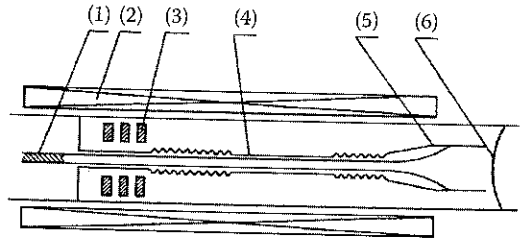

FIGURE 10.30
CARM from the Institute of Applied Physics: (1) cathode, (2) pulsed axial field coil, (3) slotted copper rings, (4) resonator with rippled-wall Bragg reflectors, (5) beam collector, and (6) vacuum window.

field extending from the cathode of the foil-less diode through the interaction cavity. To provide the perpendicular velocity for the beam electrons, a magnetic field wiggler was created by placing three slotted copper rings downstream of the diode with a spacing equal to the Larmor pitch of the beam electrons. Values of $\beta_\perp$ between 0.2 and 0.4 were produced in this manner with a spread of 0.05. The resonator had Bragg mirrors on either end of the interaction region[96]; the diffractive and ohmic Qs for the TE_{41} mode in this cavity were 3000 and 1000, respectively. At $\beta_\perp = 0.2$, the computed starting current for oscillation was 300 A, while the calculated efficiency was 4%. In experiments, a starting current of about 500 A was measured, and the 10-MW output represented an efficiency of 2%. For beam currents below the start current, there was no appreciable microwave emission.

10.3.4.2 Gyroklystrons

Gyroklystrons are the marriage of the gyrotron concept of generating microwaves using the electron cyclotron maser mechanism and the klystron concept of increasing power and efficiency by bunching a beam in one set of cavities and extracting the output from an electromagnetically isolated cavity with the high efficiency that results from the interaction with a prebunched beam. Of course, the difference from klystrons themselves is the microwave-generating mechanism and the fact that the bunching is in the rotational phase of the electrons about their guiding centers.

Significant effort has been devoted to the exploration of gyroklystrons for millimeter-wave radars at the 100-kW level; however, the investigation of high power gyroklystrons at powers approaching 100 MW has been supported by the need for a high power and high-efficiency driver for high-energy electron-positron linear colliders. This work has largely been concentrated at the University of Maryland. The highest power produced by this group — 75 to 85 MW at about 8.6 GHz with an efficiency near 32% and a gain near 30 dB in an amplifier — was described in a 1998 paper by Lawson et al.[60] The device is shown schematically in Figure 10.31. It is a coaxial device, with the center conductor supported by the two tungsten pins, intended to cut off propagation of microwaves at the TE_{01} working mode between cavities. Additional absorber, lossy ceramics made of carbon-impregnated aluminosilicate (CIAS) and 80% BeO/20% SiC, is used to further prevent the propagation of the parasitic, lowest-order TE_{11} mode between cavities; nominal attenuation in the drift tube for this mode in the X-band was 4.7 dB/cm (see Problem 13). The parameters of this device are summarized in Table 10.1. The electron beam is produced in a magnetron injection gun (MIG) that was designed using the EGUN simulation code. Simulations showed that the efficiency of the device declined slowly and monotonically with axial velocity spread, although with the spread shown in the table, the reduction was only about 1%. The output cavity was formed by changing the radius on both the inner and outer walls, and it is bounded on the right by a lip with radii matching those of the upstream drift tube.

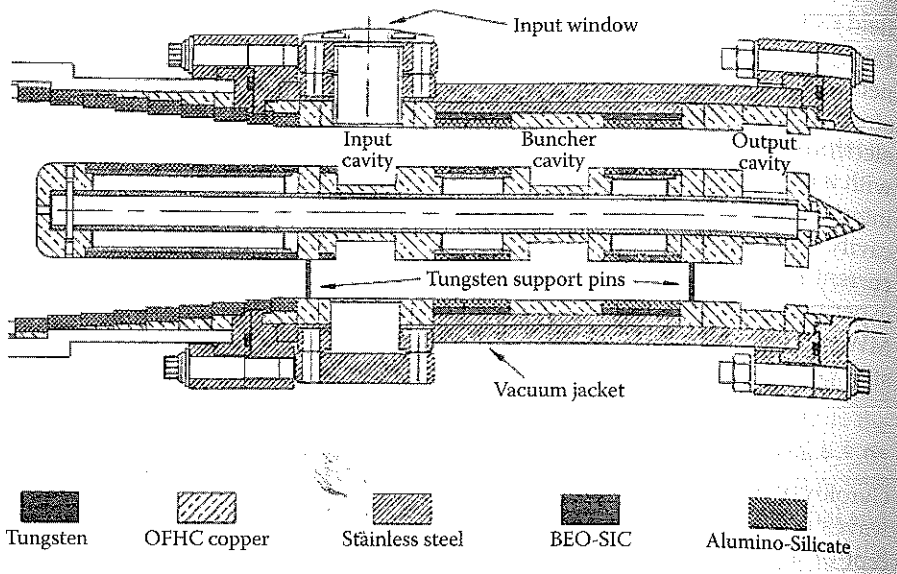

FIGURE 10.31
Schematic of the three-cavity microwave circuit for the 80-MW gyroklystron amplifier from the University of Maryland. (From Lawson, W. et al., *Phys. Rev. Lett.*, 81, 3030, 1998. With permission.)

The Q of the input cavity was determined by the combination of the diffractive Q of the input aperture and the ohmic Q of the cavity, while the Q of the buncher cavity was determined by ohmic losses in the nearby absorbing ceramics. The Q of the output cavity was essentially a diffractive Q that could be adjusted by changing the length of the lip at the right of the cavity. Figure 10.32 shows the voltage and current waveforms and microwave output envelope. We note the relative constancy of these parameters in comparison, for example, to the much higher voltage, current, and power traces of a pulse-line-driven experiment such as that shown in Figure 10.26 and Figure 10.27. The gyroklystron gun was driven by a modulator, and mismatches there were the source of the voltage drop in Figure 10.32. Also, the noise on the pulses, particularly notable in the output envelope, was attributed to ground-loop noise.

Subsequent work on this gyroklystron has concentrated on the production of a higher-frequency version operating at 17.1 GHz.[97] The rationale for increasing the frequency was the scaling for the number of sources required to drive a linear electron-positron collider of a given energy: if power and pulse length can be held constant as the frequency f increases, the number of sources decreases as $1/f^2$. The follow-on four-cavity design featured a TE_{011} input cavity driven at half the output frequency, followed by three cavities operating in the TE_{021} with frequency doubling to 17.1 GHz. The device operated at the second harmonic of the cyclotron frequency, allowing a lower magnetic field to be used. An output power of

TABLE 10.1

System Parameters at the Nominal Operating Point for the University of Maryland Gyroklystron Shown in Figure 10.31

Magnetic Field Parameters		Output Cavity Parameters	
Cathode axial field (T)	0.059	Inner radius (cm)	1.01
Input cavity field (T)	0.569	Outer radius (cm)	3.59
Buncher cavity field (T)	0.538	Length (cm)	1.70
Output cavity field (T)	0.499	Quality factor	135 ± 10
		Cold resonant frequency (GHz)	8.565
Input Cavity Parameters		Lip length (cm)	0.90
Inner radius (cm)	1.10	*Beam Parameters*	
Outer radius (cm)	3.33		
Length (cm)	2.29	Beam voltage (kV)	470
Quality factor	73 ± 10	Beam current (A)	505
Cold resonant frequency (GHz)	8.566	Average velocity ratio (α)	1.05
		Axial velocity spread (%)	4.4
Drift Tube Parameters		Average beam radius (cm)	2.38
Inner radius (cm)	1.83	Beam thickness (cm)	1.01
Outer radius (cm)	3.33	*Amplifier Results*	
Length, input to buncher (cm)	5.18		
Length, buncher to output (cm)	5.82	Drive frequency (GHz)	8.60
		Output power (MW)	75
Buncher Cavity Parameters		Pulse length (μsec)	1.7
		Efficiency (%)	31.5
Inner radius (cm)	1.10	Gain (dB)	29.7
Outer radius (cm)	3.33		
Length (cm)	2.29		
Quality factor	75 ± 10		
Cold resonant frequency (GHz)	8.563		

100 MW was planned, although problems with the electron gun limited the output in early experiments.

Lawson considered the general issue of frequency scaling for devices of this type in a 2002 paper that looked at 100-MW class K_u-band (17-GHz), K_a-band (34-GHz), and W-band (91-GHz) devices.[98] He concluded that for a number of reasons — cathode loading, beam axial spread caused by increasing magnetic compression of the beam, $f^{5/2}$ scaling of cavity wall power losses in circular modes, manufacturing tolerances, and mode competition in the W-band — that the gyroklystron as it has been designed is probably viable up to the K_a-band, around 34 GHz.

Another issue with general application for devices of this type is beam uniformity in MIGs with thermionic cathodes. Variations in the temperature and in the local work function for emission contribute to beam nonuniformities that can drive beam tunnel instabilities where none are expected. Consequently, the group at the University of Maryland is exploring the design of a space-charge-limited, rather than temperature-limited, electron gun.[99]

Additional prototype experiments at the NRL with a different gyroklystron illustrated another strength of this type of device in achieving phase locking

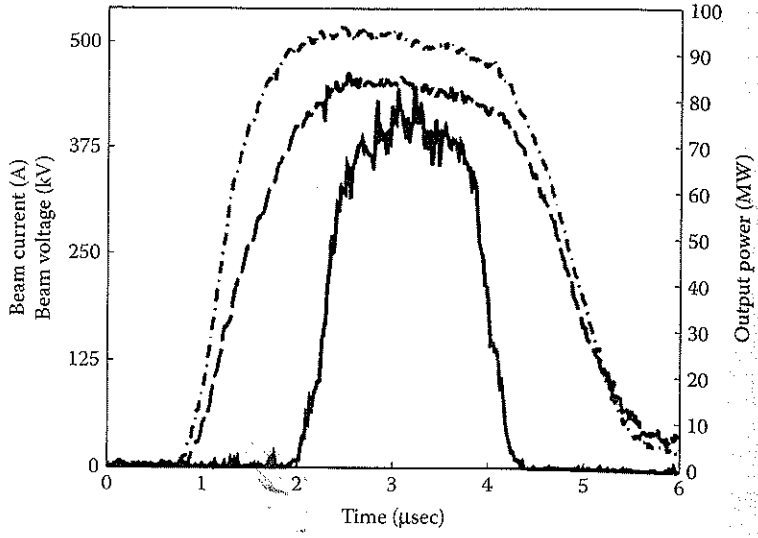

FIGURE 10.32
Voltage (dashed line), current (dash–dot line), and microwave output envelope (solid line) waveforms from the gyroklystron experiment of Figure 10.31. (From Lawson, W. et al., *Phys. Rev. Lett.*, 81, 3030, 1998. With permission.)

of multiple sources.[100] In a single-cavity device, the fractional bandwidth over which phase locking can occur, $\Delta f/f$, is related to the external Q of the cavity, the drive power of the input, P_i, and the output power, P_o, and is given by the Adler inequality (Equation 10.14). Theory shows, though, that injection of the drive signal into a prebunching cavity in a gyroklystron allows a wider phase-locking bandwidth than Adler's inequality would. This prediction was tested in a prototype experiment with the results shown in Figure 10.33. Note that for injection into the third of three cavities, the phase-locking points fall very near the Adler curve. For injection into the input cavity (results plotted in the lower graph), the power required to achieve a given bandwidth is lower than the value indicated by Adler's relation.

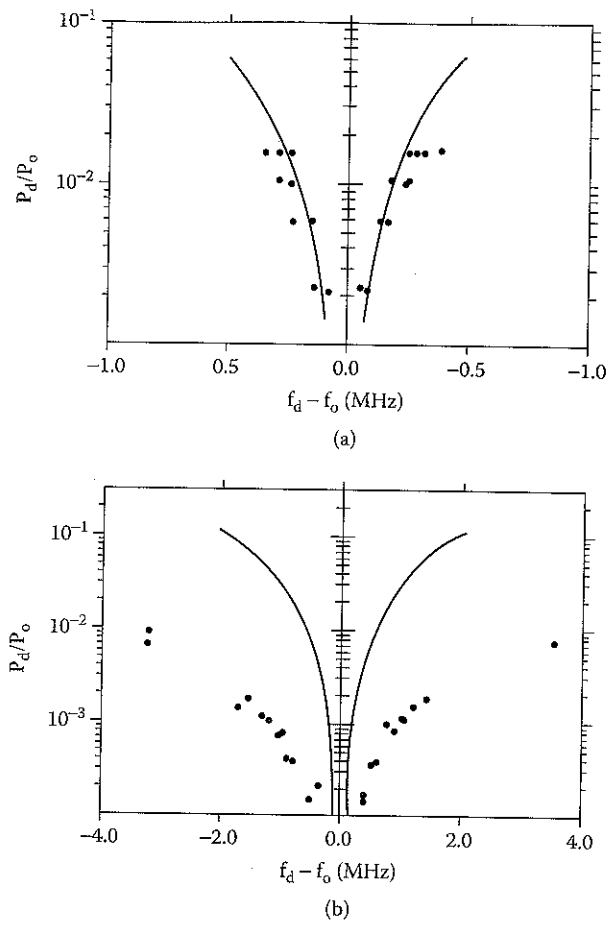

FIGURE 10.33
Phase-locking bandwidth for (a) direct injection to a cavity with an external Q of 1100 and (b) injection into a three-cavity gyroklystron with a final cavity external Q of 375. The solid line is the prediction from Adler's inequality. (From McCurdy, A.H. et al., *Phys. Rev. Lett.*, 57, 2379, 1986. With permission.)

10.3.5 Outlook for Electron Cyclotron Masers

Research and development in this class of sources continues to be dominated by 1- to 2-MW-class gyrotrons in the 100- to 200-GHz range for use in magnetic confinement fusion experiments. The developments achieved by an international group of organizations from Russia, Germany, France, the U.S., and Japan have been remarkable over the past decade. Notably, the accomplishments of this effort have included the use and mode control of very high order azimuthal modes in cavities that are tens of free-space wavelengths in diameter; the development and routine inclusion of integrated quasi-optical output couplers that allow the separation of this task from beam collection; and the continued development of chemical vapor deposition (CVD) artificial diamond windows to get the strength, low loss tangent, and thermal conductivity required for the high power fluxes they must transmit. This last element is particularly important, because the failure of a window breaks the vacuum of the assembly, which not only compromises its cleanliness, but also destroys the cathodes in the electron guns.

Gyroklystrons provide an alternative to klystrons for X-band amplifiers with power in the 100-MW regime and pulse lengths of the order of a microsecond. At higher frequencies, in the K_u- and K_a-bands (up to 35 GHz, roughly), they quite possibly provide the superior alternative to klystrons. As with klystrons, the future development of these sources, at least at this

power level, might be called into question by the demise of the Next Linear Collider concept in favor of the International Linear Collider, with lower power and frequency requirements. Radar and other applications, however, might continue to drive the development of this source at lower power levels.

CARMs offer an interesting possibility for the production of high-frequency sources in the HPM regime. Nevertheless, at this point, they remain immature, with relatively little development, and it could be that the requirement they pose for high beam quality could limit the prospects for changing this situation.

10.4 Free-Electron Lasers

Free-electron lasers (FELs) offer an almost unlimited frequency range, and in this regard they are the highest-frequency producer of gigawatt-level microwave power, with an output of 2 GW at 140 GHz while firing repetitively and achieving some tens of percent efficiencies. This remarkable performance comes at a cost in size and volume: FELs require very high beam quality, which militates against high-current, and toward high-voltage, operation. In addition, they are relatively complex sources. More compact devices operating at lower frequencies in the high-current Raman regime with applied axial magnetic fields have been demonstrated as well. All of these sources operate as amplifiers, and as such, they provide tunable alternatives to relativistic klystrons and gyroklystrons for applications with frequency requirements above the X-band. A number of reviews of the field are available, for example, Freund and Antonsen.[101]

10.4.1 History

Although the possibility of using the Doppler upshift of radiation to achieve very high frequencies was realized as early as the 1930s by Kapitsa and Dirac,[102] followed by the recognition that Doppler-upshifted undulator radiation could be used to generate coherent millimeter-wave output,[103] the serious development of the FEL occurred on two fronts, beginning with R.M. Phillips in the late 1950s. Working at the General Electric Microwave Laboratory in Palo Alto, he experimented with the ubitron,[104] a device using a permanent magnet undulator. This work produced a number of megawatt-class devices, both amplifiers and oscillators, at frequencies between 2.5 and 15.7 GHz.

On the second front, researchers at Stanford using higher-energy, lower-current beams from a linear accelerator developed the device they called a free-electron laser. Madey proposed his concept in 1971,[105] and an amplifier

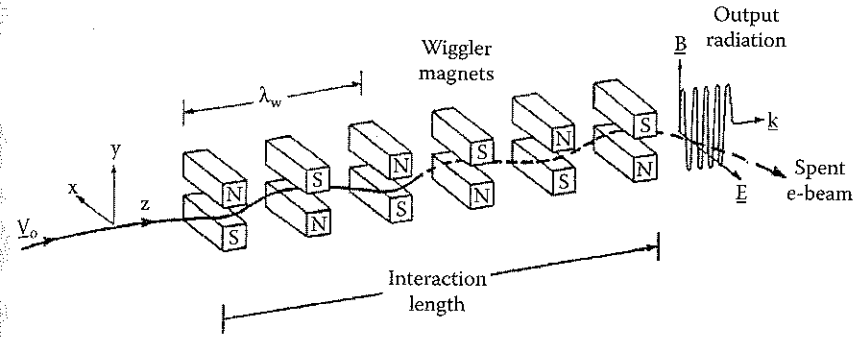

FIGURE 10.34
The basic FEL configuration. Beam electrons undulate in the periodic magnetic field of the wiggler. The electrons radiate and bunch in the ponderomotive potential well formed in the combination of pump and radiation fields.

of 10.6-μm light was announced in 1976.[106] A year later saw the achievement of laser oscillation at 3.4 μm.[107]

In the 1970s, work continued in the microwave and millimeter-wave regimes, with the production of some tens of megawatts of power by groups at the NRL, the Khar'kov Physico-Technical Institute, the Lebedev Institute and the Institute of Applied Physics, and Columbia University. In the 1980s, work continued on relatively high-current FELs at the NRL and MIT, notably, while lower-current, higher-energy beams were employed at the Lawrence Livermore National Laboratory (LLNL) to produce 1 GW at 35 GHz, followed later by 2 GW at 140 GHz, which is the highest brightness experiment conducted, by the measure of the product of power and the square of the frequency, Pf^2. These latter experiments, which we will describe in detail later, also involved the generation of 1-GW pulses at a repetition rate up to several kilohertz.

The LLNL experiments have been discontinued, but work continues in Russia with the Budker Institute of Nuclear Physics in Novosibirsk producing hundreds of megawatts in millimeter-wave radiation in work also involving the Institute of Applied Physics. Also, at the Institute of Applied Physics, the SINUS-6 generator has been employed in research on a new type of FEL concept that has produced power levels approaching 10 MW.

10.4.2 Free-Electron Laser Design Principles

An FEL is configured as shown in Figure 10.34. An electron beam with a z-directed velocity $v_z = v_0$ at the input is injected into a wiggler* magnetic field with a period λ_w. On the axis, the y component of the wiggler magnetic field

*There is some debate about the uses of the terms *undulator* and *wiggler* for the periodic magnet inducing radiation in an FEL. We simply use the term *wiggler* everywhere without apology.

deflects the electrons in the x direction. This oscillatory motion has a wavenumber k_w and a wiggle frequency Ω_w given by

$$k_w = \frac{2\pi}{\lambda_w} \tag{10.23a}$$

$$\Omega_w = k_w v_z \tag{10.23b}$$

and the transverse acceleration of the moving charges results in forward-directed radiation. The beating of the radiation with wavenumber k_w and frequency ω with the "pump" field of the wiggler creates a potential well (known as the *ponderomotive* potential well[108]) moving at a phase velocity $\omega/(k_z + k_w)$, within which the electrons form bunches. It is this bunching that enforces the coherence of the emitted radiation.

The relationship between the wavelength of the wiggler and the wavelength and frequency of the output radiation is determined approximately from the location of the resonant interaction between the dispersion curves for the Doppler-shifted electron oscillation, which is the wiggler-shifted slow space-charge wave on the beam, and an electromagnetic normal mode. As an initial cut at this estimate, we assume first that the beam density is low and use a wiggler-shifted beam line to approximate the space-charge wave:

$$\omega = \left(k_z + k_w\right) v_z \tag{10.24}$$

For convenience, we approximate the dispersion curve of the electromagnetic wave by the free-space dispersion relation for a wave traveling along the z axis, thus ignoring the effect of the cutoff frequency for $\omega >> \omega_{co}$:

$$\omega = k_z c \tag{10.25}$$

In Equation 10.24, note that the wiggler shift is shown by the addition of k_w to k_z, and that the space-charge term splitting the fast and slow space-charge waves has been omitted, consistent with our assumption of low beam density. The simultaneous solution of Equations 10.24 and 10.25 provides the frequency and wavenumber at which resonance occurs:

$$\omega_{res} = \left(1 + \beta_z\right) \frac{\Omega_w}{1 - \beta_z^2} \tag{10.26}$$

with $\beta_z = v_z/c$. Using the definition of the relativistic factor γ, we write

$$1 - \beta_z^2 = \frac{1}{\gamma^2}\left(1 + \beta_x^2 \gamma^2\right) \tag{10.27}$$

Here, given that the wiggler induces electron motion in the x-z plane, $\beta_x = v_x/c$. This transverse wiggle velocity is calculated from the equation of motion, using the fact that for a time-independent wiggler field, $d/dt = v_z(d/dz)$, and assuming a planar wiggler with $B_w \sin(k_w z)$ the y component of the field:

$$v_z \frac{d\left(\gamma\beta_x\right)}{dz} = \frac{e}{mc} v_z B_w \sin\left(k_w z\right) \tag{10.28}$$

This equation is integrated straightforwardly, and the result has a z dependence of $\cos(k_w z)$. Rather than reinsert this term into Equation 10.27, we use the spatial average, with $\langle\cos^2(k_w z)\rangle = 1/2$:

$$\left\langle \gamma^2 \beta_x^2 \right\rangle = \frac{1}{2}\left(\frac{eB_w}{mck_w}\right)^2 \equiv \frac{1}{2} a_w^2 \tag{10.29}$$

Finally, using the fact that $k_z = 2\pi/\lambda$ in free space and $k_w = 2\pi/\lambda_w$, Equations 10.26, 10.27, and 10.29 are combined to yield the characteristic wavelength of the FEL output:

$$\lambda = \frac{\lambda_w}{\beta_z\left(1 + \beta_z\right)\gamma^2}\left(1 + \frac{1}{2} a_w^2\right) \approx \frac{\lambda_w}{2\gamma^2}\left(1 + \frac{1}{2} a_w^2\right) \tag{10.30}$$

In the latter expression, we have made the common replacement as β_z approaches unity for large electron energies, but we note that at the lower energies common for microwave experiments this approximation could introduce some error. Our derivation was for planar wigglers, but the same relation holds for helical wigglers, except without the factor of 1/2 prior to a_w^2, provided B_w represents the peak value of the field. Equation 10.30 is an important relationship, given the output wavelength as a function of γ, λ_w and b_w. Note that the strong energy dependence of the output frequency, as γ^2, makes device operation very sensitive to spreads in the energy of the electrons in the driving beam. Electrons at energies other than the resonant energy do not contribute to microwave generation at the predominant output frequency. As a consequence, FELs demand a beam of relatively low emittance for efficient operation; this requirement becomes increasingly stringent at shorter wavelengths.

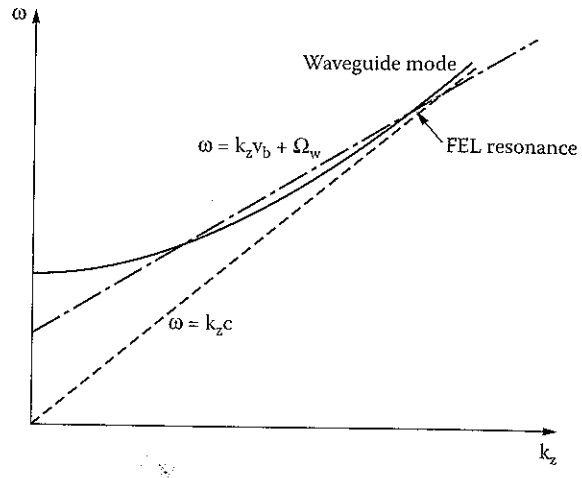

FIGURE 10.35
The uncoupled dispersion curves for a waveguide mode given by $\omega^2 = k_z^2c^2 + \omega_{co}^2$ (which is asymptotic to the light line, $\omega = k_z c$) and the wiggler-shifted beam line of Equation 10.24.

Our derivation of Equation 10.30 ignored three important features of many HPM FELs: (1) the fact that the electromagnetic normal modes involved in the interaction are actually waveguide or cavity normal modes (see Problem 15), (2) the effect of beam space-charge, and (3) the application of a constant axial magnetic field in many devices. With regard to the first topic, we note that the beam in an FEL can interact with either TE or TM modes; in fact, at high currents, the transverse displacement of the beam couples the TE and TM modes. In general, the wiggler-shifted beam line will intersect a hyperbolic waveguide mode dispersion curve in two places, as illustrated in Figure 10.35. The existence of these two resonances has been experimentally verified.[109] The experimental scaling of the upper resonant frequency with beam energy and the wiggler field is shown in Figure 10.36.[110] In Figure 10.36a, the calculated resonance frequencies for the TE_{11} and TM_{01} modes are compared with output frequencies measured in experiments at the NRL. In Figure 10.36b, the power measured in separate frequency bands using a millimeter-wave grazing spectrometer with a resolution of about 1 GHz is shown; note that as the wiggler field increases in magnitude, the peak power shifts to lower frequencies, consistent with Equation 10.30.

The issue of selecting between the higher- and lower-frequency modes in an FEL is treated elsewhere.[111] The lower-frequency resonance occurs at a point of negative group velocity on the waveguide mode if $\Omega_w > \omega_{co}$. This is potentially problematic, because this interaction with a negative-group-velocity mode can support an absolute instability, which can grow in place to large amplitudes.[112] Possible solutions include modifying the wiggler frequency to push it below the cutoff frequency and keeping the wiggler below a critical length to prevent the oscillation from exceeding its start-current threshold[113] (see Problem 16). In many instances, the lower-frequency

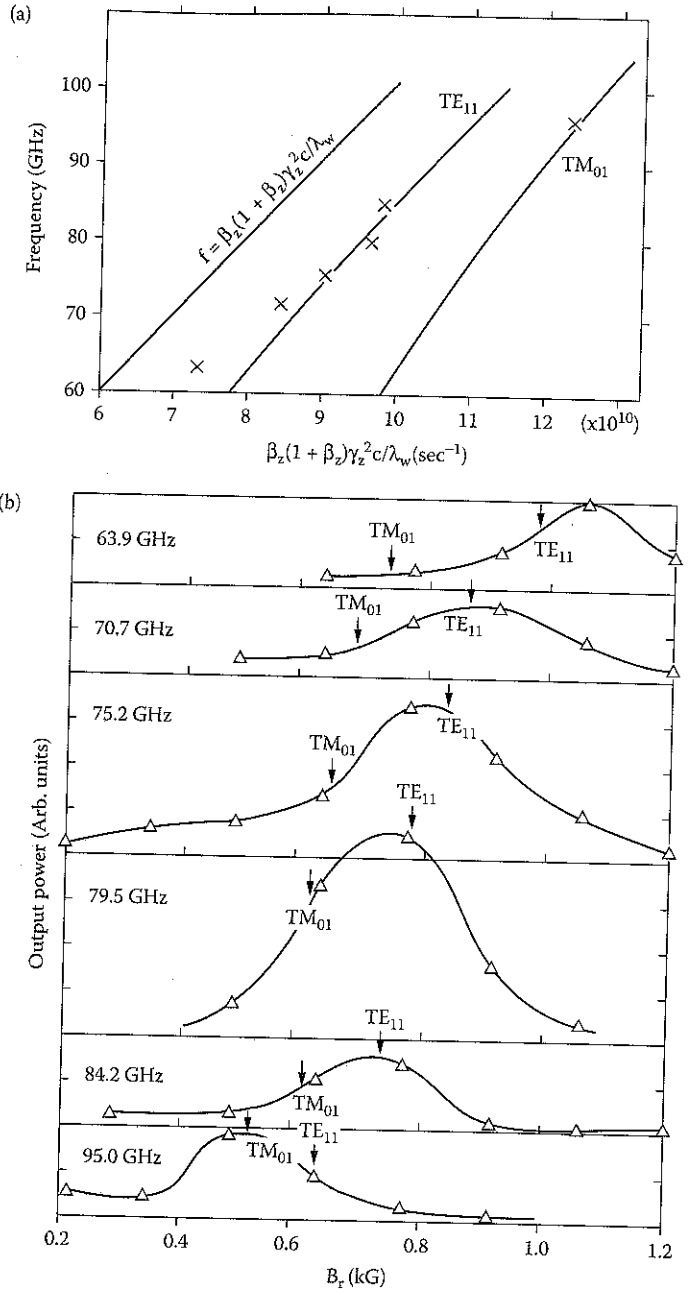

FIGURE 10.36
(a) Solid curves: calculated FEL resonances with the light line and the TE_{11} and TM_{01} waveguide modes. Xs: experimentally determined operating points in the reference. (b) FEL output power (in arbitrary units) in six detector bands as a function of the wiggler field, B_r. (From Gold, S.H. et al., *Phys. Fluids*, 26, 2683, 1983. With permission.)

absolute instability will grow more slowly than the FEL interaction, preventing it from becoming a problem in short-pulse devices.[114]

Space-charge effects are particularly important at microwave frequencies, because many of the experiments in this frequency range use intense electron beams. Depending on the strength of the space-charge and wiggler effects, three regimes of FEL operation are identified: the *Compton*, *Raman*, and *strong-pump* or *high-gain Compton* regimes.[115] In the Compton regime, the electron beam current and space-charge are very low, coherent single-particle effects dominate, and device gain is low. Compton operation is most appropriate for experiments performed at high energies for wavelengths much shorter than those in the microwave spectrum. The Raman regime is applicable to intense beam experiments where the high space-charge plays a dominant role in the interaction. In this case, the frequencies of the wiggler-shifted fast and slow space-charge waves are split about the frequency given in Equation 10.24, and the interaction occurs at the lower frequency. The strong pump regime is applicable to cases where the effect of a very strong wiggler field overpowers space-charge effects in an otherwise intense electron beam.

The application of an axial magnetic field B_z aids in the transport of the intense electron beam through an FEL. It also has a significant effect on the electron trajectories and, consequently, on the output. A calculation of the single-particle trajectories shows them to be of two types, called group I and group II.[116] For both types, the wiggle velocity perpendicular to the z axis has the magnitude

$$v_w = \frac{\Omega_w}{\gamma\left(\Omega_0 - \Omega_w\right)} v_z \tag{10.31}$$

where $\Omega_0 = eB_z/m\gamma$. The difference between the two orbit types lies in the dependence of v_z on B_z, as shown in Figure 10.37.[117] The calculation from which the plot was taken was for a helical wiggler, assuming the form of an ideal wiggler using only the on-axis fields, and an actual wiggler, taking account of the off-axis variation of the fields. Group I orbits occur at low values of the magnetic field, for which $\Omega_0 < \Omega_w$, and have high axial velocities that decline with B_z until the orbits become unstable, when $\Omega_0 = \Omega_w/(1 - v_w^2/v_z^2)$. The ideal group II orbits exist for all positive values of B_z, with an axial velocity that increases with the axial field and is large only at large axial fields. The resonance $\Omega_0 = \Omega_w$ does not occur for either group of trajectories, but it can be approached, in which case the transverse wiggle velocity becomes large, according to Equation 10.31, as does the FEL gain.[118,119] An additional feature of interest is that for smaller values of B_z, electrons with group II orbits have a negative mass characteristic, in that the axial velocity actually *increases* as the energy decreases: $\partial\beta_z/\partial\gamma < 0$. As the axial field increases, however, the sign of the derivative eventually changes. At the lower field values, the interaction between a beam of group II electrons and the electromagnetic field is more complicated, with both space-charge and

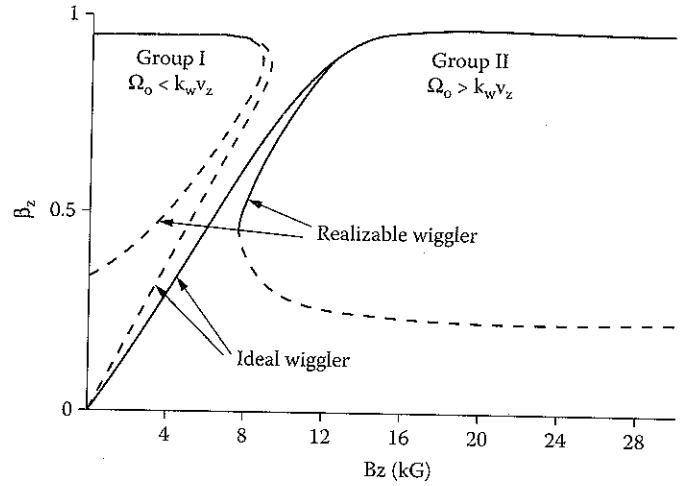

FIGURE 10.37
An example of the variation of β_z with the axial magnetic field for group I and group II orbits. Calculations were made for both ideal wiggler fields and realizable wigglers, taking account of the off-axis variation of the fields. (From Jackson, R.H. et al., *IEEE J. Quantum Electron.*, QE-19, 346, 1983. With permission.)

modified cyclotron wave interactions producing wave growth.[118] Experimental results indicate that even higher power can be achieved by reversing the axial field, in the sense that the cyclotron motion of the electrons in the axial field has an opposite rotational sense than the motion in the wiggler field (removing the possibility of a wiggler cyclotron resonance, since $\Omega_0 < 0$).[120]

The growth of electromagnetic waves in an FEL occurs at the expense of the kinetic energy of the beam electrons. The beating of the signal against the wiggler field pump forms a ponderomotive potential with phase velocity $\omega/(k_z + k_w)$. As the electrons lose energy and the ponderomotive potential wells deepen, the electrons' axial velocity drops to the phase velocity of the ponderomotive potential, and some fraction of the electrons are trapped in the potential wells. The process is depicted in the schematic phase-space plot of Figure 10.38.[121] Trapping is seen in the swirling of electrons near the bottom of the ponderomotive potential well. The axial velocity of the trapped electrons oscillates about the ponderomotive or space-charge wave phase velocity. This periodic variation, known as *synchrotron oscillations*, is governed by a nonlinear pendulum equation.[108] Figure 10.39 illustrates the effect of these trapped electrons on the saturated signal: note the variation in the signal amplitude after it reaches its maximum.[122] This is due to the periodic exchange of energy between the wave and the trapped electrons, with the faster of either the wave or the trapped electron accepting energy from the other at any point in the synchrotron oscillation period.

The output power and efficiency of an FEL can be further increased after the onset of trapping by continuing to extract energy from the trapped electrons. This is done by decreasing the phase velocity of the ponderomotive

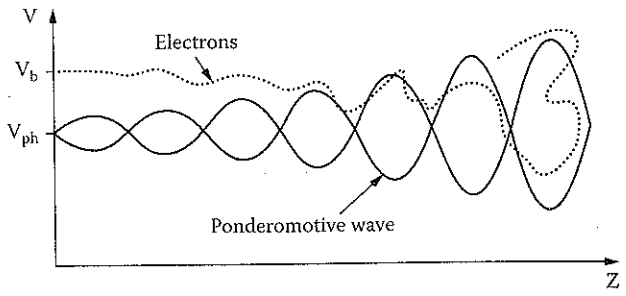

FIGURE 10.38
A schematic phase-space plot of electrons in an FEL illustrating the energy loss and eventual trapping in the growing ponderomotive potential well of the pump and radiation fields. (From Pasour, J.A., *High-Power Microwave Sources*, Granatstein, V.L. and Alexeff, I., Eds., Artech House, Norwood, MA, 1987. With permission.)

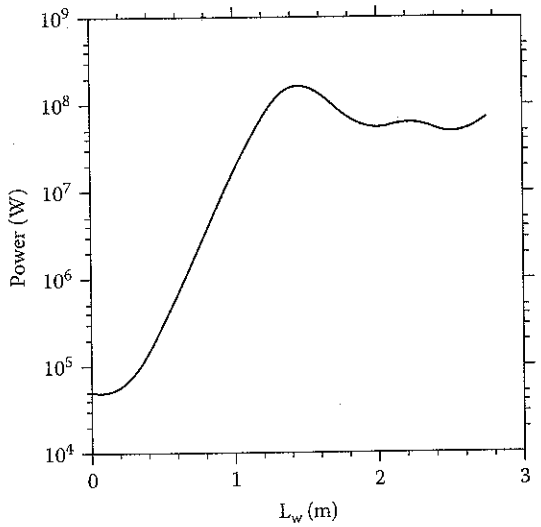

FIGURE 10.39
The growth and saturation of the microwave signal as a function of distance from the input end of an FEL amplifier. Note the small-signal or linear regime of exponential signal growth between 0.4 and 1.4 m and the saturation at peak amplitude. (From Orzechowski, T.J. et al., *Nucl. Instrum. Methods*, A250, 144, 1986. With permission.)

potential; the trapped electrons are slowed as well, surrendering further energy to the electromagnetic wave. Alternatively, in terms of Equation 10.30, as γ decreases for the electrons, signal growth at a fixed wavelength can be maintained if either the wiggler period or the wiggler field magnitude is decreased accordingly. In either case, the process of varying the wiggler parameters is known as *wiggler tapering*. In FELs with an applied axial magnetic field, wiggler tapering becomes more complex, with the added option of tapering the axial field as well to increase the power. The reader seeking more information on this topic is directed to Freund and Ganguly.[123]

Since wiggler tapering increases the power and efficiency of an FEL by extracting energy from the trapped portion of the electron population, it is important to ensure that these electrons remain trapped during the extraction process. One cause of detrapping is the use of an overly rapid taper in the wiggler parameters. A second cause is the *sideband instability*.[124–126] This is a nonlinear interaction between the FEL signal at frequency ω_0 and the synchrotron oscillations of the trapped electrons at ω_{syn}, resulting in the formation of sidebands at $\omega_0 \pm \omega_{syn}$ that grow at the expense of the main output signal. The frequency spacing between the sideband and the signal is roughly[127,128]

$$\Delta\omega = \frac{k_{syn}c}{1 - v_z v_g} \tag{10.32}$$

where v_g is the group velocity of the signal at ω_0 and

$$k_{syn} = \left(\frac{e^2 E_s B_w}{\gamma_z^2 m^2 c^3}\right)^{1/2} \tag{10.33}$$

with E_s the peak electric field of the microwaves and γ_z the resonant value of γ found in Equation 10.30, given λ, λ_w, and a_w. An example of a signal with a sideband in a long constant-parameter wiggler is shown in Figure 10.40.[129] There, the shorter wavelength signal is due to the main FEL resonance, while, of the two possible sidebands, that with the longer wavelength is the one observed. The dashed curve shown in the figure is the computed spatial growth rate of the FEL interaction as a function of wavelength; note that strong sideband formation does not require the main FEL interaction to have growth at the sideband wavelength. The peak power in the main signal and the sideband is plotted as a function of the wiggler field in Figure 10.41. There note the threshold value of the field for FEL output, the analog of the start current in the case of a fixed beam current, and the growth of the sideband power with the wiggler strength.

10.4.3 Operational Features of Free-Electron Lasers

A number of interesting microwave FEL experiments have been performed, but we limit ourselves to the discussion of three: the extraordinarily high brightness experiments, measured by the product Pf^2, conducted on the Experimental Test Accelerator (ETA) at Livermore; a microwave proof of principle of the optical klystron configuration at MIT; and the experiments at the Budker Institute of Nuclear Physics in Novosibirsk.

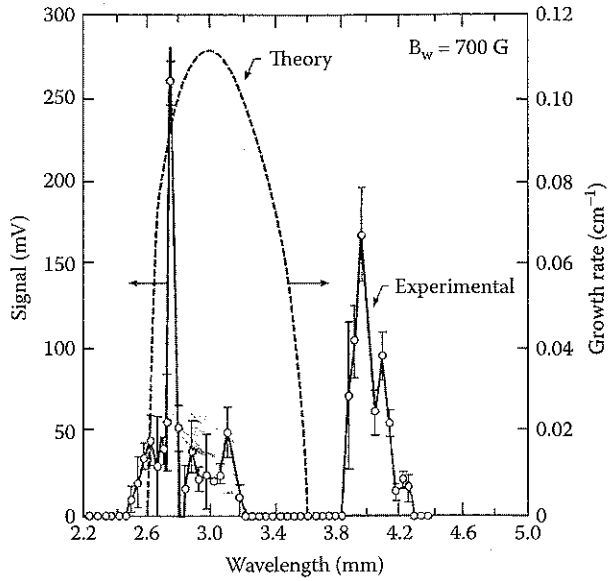

FIGURE 10.40
Spectral output of an FEL with strong sideband growth. The tall peak at shorter wavelength is the main signal, while the peak on its long-wavelength side is the sideband. The dashed curve is the calculated spatial growth rate. (From Yee, F.G. et al., *Nucl. Instrum. Methods*, A259, 104, 1987. With permission.)

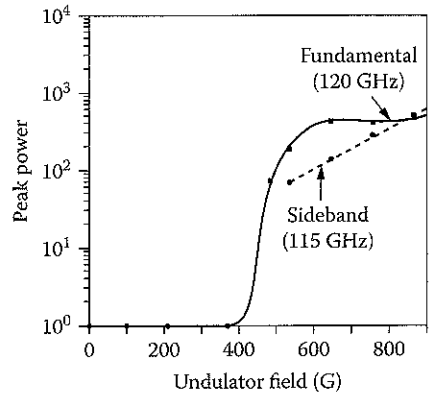

FIGURE 10.41
Power at the main signal frequency and in the sideband as a function of wiggler field in the same experiments as Figure 10.40. (From Yee, F.G. et al., *Nucl. Instrum. Methods*, A259, 104, 1987. With permission.)

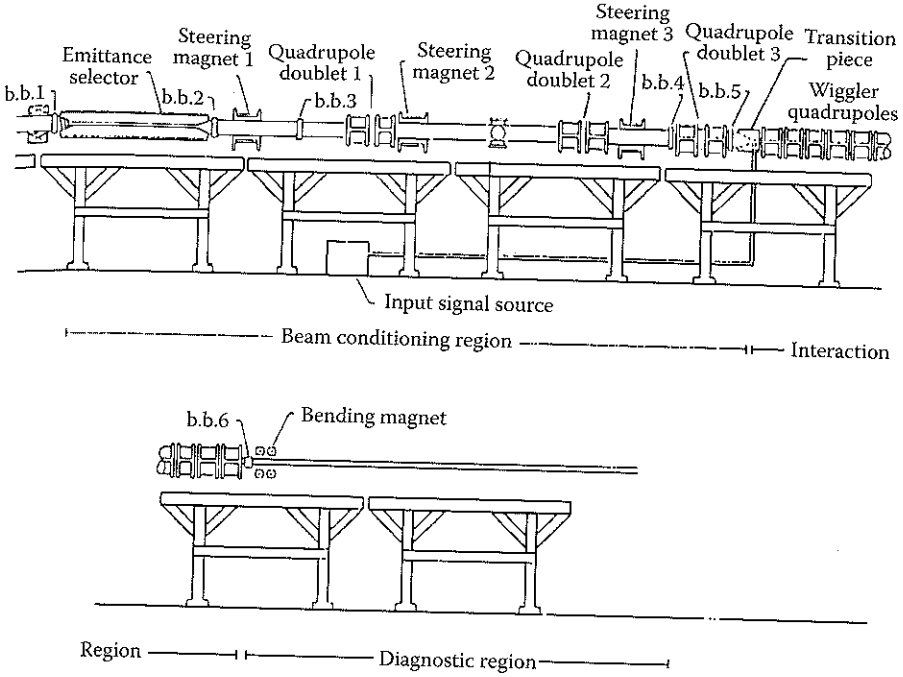

FIGURE 10.42
Layout of the FEL amplifier experiments at LLNL, from the emittance selector beam input to the downstream diagnostic chamber. (From Throop, A.L. et al., Experimental Characteristic of a High-Gain Free-Electron Laser Amplifier Operating at 8-mm and 2-mm Wavelengths, UCRL-95670, Lawrence Livermore National Laboratory, Livermore, CA, 1987. With permission.)

The FEL experiments at LLNL, involving a collaboration with researchers from the Lawrence Berkeley Laboratory (LBL, now the Lawrence Berkeley National Laboratory) as well, produced a remarkable series of results culminating in the production of 2 GW at 140 GHz. The layout of the FEL itself is shown in Figure 10.42,[130] which illustrates the complexity of the FEL. The accelerators creating the electron beam were multicell, linear induction accelerators known as the Experimental Test Accelerator (ETA) and the follow-on ETA II upgrade; both were similarly large and complex. ETA was capable of producing a 4.5-MeV, 10-kA, 30-nsec electron beam[131]; however, at the wavelengths involved, the LLNL FEL required a high-quality, low-emittance electron beam. In order to improve the beam quality by reducing its emittance, the ETA beam was passed into the emittance selector shown at the left of the figure. This was essentially a long, smaller-radius waveguide section that scraped off electrons at large radii and large angular divergence. The maximum normalized emittance acceptance of the selector was 4×10^{-3} π rad-m, and a transmitted 1.6-kA, 10- to 15-nsec beam had a brightness of 2×10^8 A/(m-rad)^2. Downstream of the selector, steering and quadrupole magnets matched the beam to the planar wiggler. Built of pulsed (1-msec)

air-core electromagnets with a period $\lambda_w = 9.8$ cm, the original wiggler had a total length of 3 m (later increased to 4 m) and peak amplitudes of 0.37 T ($a_w = 2.4$) for experiments at 35 GHz and 0.17 T ($a_w = 1.1$) for experiments at 140 GHz. Independent variation of the wiggler field for each of the two periods allowed for tapering of the wiggler strength at constant λ_w. At the highest power levels, optimization of the tapering profile was performed empirically. There was no axial magnetic field; horizontal focusing of the electron beam was provided by the quadrupole doublets. The microwave interaction region was a rectangular stainless steel waveguide with a cross section of 3×10 cm^2.

The keys to maximizing the output power of the Livermore FEL were, first, to minimize the emittance and beam velocity spread so that substantial numbers of electrons would be trapped in the ponderomotive pontential wells and, second, to taper the parameters of the wiggler to continue to draw upon the energy of the trapped electrons. As the beam energy and γ decrease, a corresponding decrease in a_w, as seen in Equation 10.30, can maintain a constant-wavelength resonance condition. Obviously, smaller initial spreads in the electron energies improve the usefulness of this technique by reducing thermal spreading of the trapped bunches. Tapering of the wiggler amplitude at constant λ_w was responsible for raising the output power of the LLNL/LBL FEL from 180 MW without tapering to 1 GW, as shown in Figure 10.43.[132] In terms of the current that entered the wiggler after passage through the emittance filter (Figure 10.42), 850 A at 3.5 MeV, the efficiency was raised from 6% without tapering to 35%. Note that the linear gain over the first 120 cm was about the same in either case: 0.27 dB/cm.[122] The tapering profile for the wiggler is shown in Figure 10.44 (see Problem 17). Significantly, the wiggler tapering does not begin until near the point of saturation of the no-taper signal, because this is the point at which the fraction of electrons trapped in the ponderomotive potential reaches its maximum. Numerical simulations indicated that about 75% of the beam electrons were trapped, and that 45% of their energy was removed.

A further improvement of ETA II, to ETA III, was used for experiments at 140 GHz.[133] The accelerator produced a 6-MeV, 2-kA beam, and peak output power of 2 GW was achieved in single pulses. Bursts of up to 50 pulses were also produced at 2 kHz. Microwave output pulses from such a 45-pulse burst are shown in Figure 10.45.[134] Although higher power levels were predicted in computer modeling of the system, the primary focus of effort was the use of the output for plasma heating in the Microwave Tokamak Experiment (MTX), so the device was not optimized.

Another means of increasing the gain within an FEL draws on a concept proposed originally by Vinokurov and Skrinskiy of the Institute of Nuclear Physics in Novosibirsk.[135] In order to enhance the low-signal gain of Compton FELs driven by high-energy electron beams, the *optical klystron* employs two wigglers separated by a dispersive section. The electron energy modulation imposed in the first wiggler section initiates beam bunching, which proceeds in the dispersive section. The output section then runs at a higher gain and

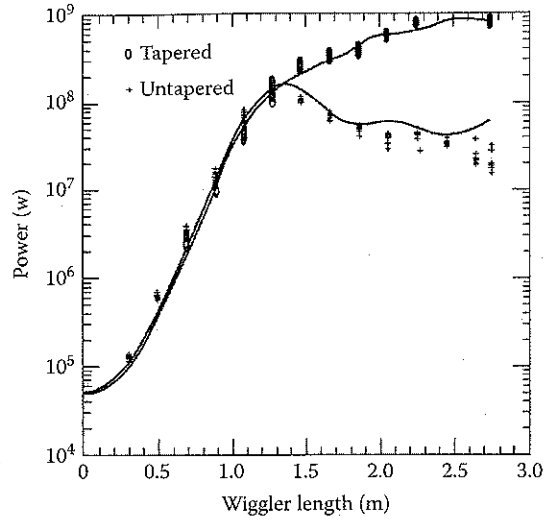

FIGURE 10.43
Microwave power in the LLNL/LBL FEL as a function of distance along the wiggler, both with and without (lower curve to the right) wiggler tapering. (From Orzechowski, T.J. et al., *Phys. Rev. Lett.*, 57, 2172, 1986. With permission.)

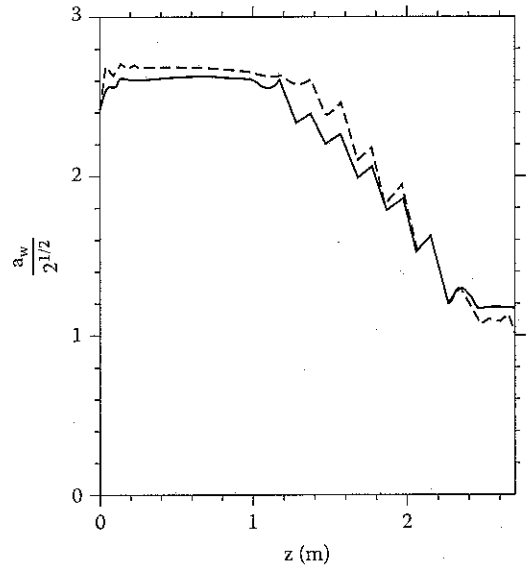

FIGURE 10.44
Axial profile of the wiggler field strength in the LLNL/LBL FEL, optimized both empirically (dashed line) and theoretically (solid line). (From Orzechowski, T.J. et al., *Phys. Rev. Lett.*, 57, 2172, 1986. With permission.)

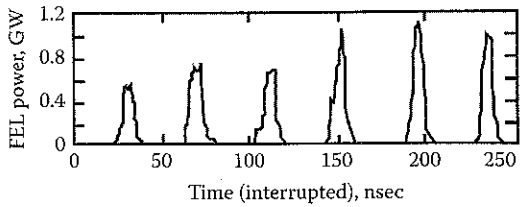

FIGURE 10.45
Pulses from a 45-shot, 2-kHz burst fired on the 140-GHz Livermore FEL powered by the ETA III accelerator. (From Lasnier, C.J. et al., Burst mode FEL with the ETA-III induction linac, in *Proceedings of the 1993 Particle Accelerator Conference*, 1993, Washington, D.C., p. 1554. With permission.)

efficiency with a prebunched beam. Although the initial experiments with this concept were conducted at high energies and short wavelengths, the concept can be adapted as well for operation at microwave frequencies, as was demonstrated in low power, proof-of-principle experiments at MIT.[136,137] A collimated electron beam with axial energy spreads of less than 0.3% passed into an interaction region that was split into two halves by a thin tungsten mesh. The mesh allowed the beam to pass almost unaffected from one half to the other, while the microwaves from the first section were attenuated by 20 dB. In the first section, an injected microwave signal was amplified, and the electron beam began to bunch. The bunched beam passed into the second section, where it began to amplify the small microwave signal that made it through the mesh. The downstream output power as a function of the effective wiggler length (Figure 10.46) was determined by using a movable kicker magnet to eject the beam from the wiggler region after traversing different distances. It must be remembered that power produced upstream of the mesh was measured downstream after it had been attenuated 20 dB by the mesh. The gain per unit length increased dramatically downstream of the mesh, from 0.069 to 0.32 dB/cm for the 188-G wiggler field, thus demonstrating the concept; however, we note that if the mesh were removed, the overall output power would be higher, despite the lower gain due to the removal of the 20-dB attenuation of the mesh. As a proof of principle, the experiment showed the applicability of the optical klystron configuration at microwave frequencies in the Raman regime of operation. Further, the technique could be used to suppress parasitic oscillations in an FEL.[138]

The FEL experiments in Novosibirsk[139] involving collaborators from the Budker Institute of Nuclear Physics and the Institute of Applied Physics in Nizhny Novgorod are interesting in three regards. First, this team has produced 200-MW, 200-J output pulses at 75 GHz. Second, they use a sheet beam — albeit with the small dimensions of 0.3 cm thickness and 12 cm width — which is often proposed, but not as often seen. Third, their system is quite rich in energy, so that they propose to produce multigigawatt output using a very large sheet beam 140 cm in width, which the authors claim has been demonstrated with this system. The weakness of the experiments

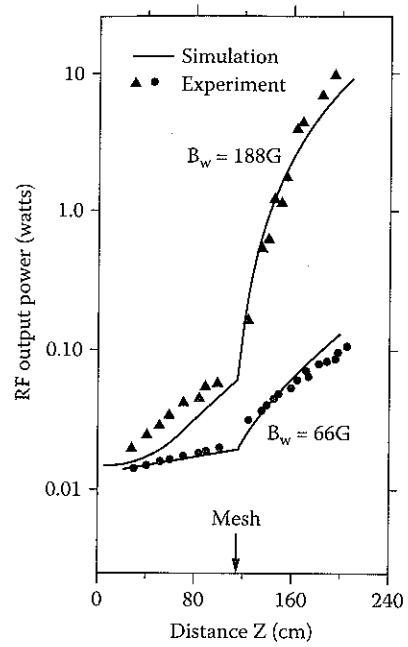

FIGURE 10.46
RF output power as a function of interaction length in the MIT experiment with a prototype optical klystron. (From Leibovitch, C. et al., *IEEE J. Quantum Electron.*, 24, 1825, 1988. With permission.)

described in their 1998 publication is that while the voltage is quite constant during a pulse, the current rises linearly for almost the full duration of the pulse. Thus, the microwave output envelope is quite irregular.

10.4.4 Outlook for Free-Electron Lasers

FELs are a very important source for the production of millimeter-wave HPM output, but the application demanding this output may not exist yet. While plasma heating was the goal for the extraordinary experiments in Livermore, the focus of the effort in support of plasma heating remains the development of long-pulse or continuous gyrotrons. Simply put, the complexity of HPM makes a high-peak-power system with rapid pulsing an uneconomical way to achieve high average power. Nevertheless, FELs retain some untapped potential. For example, the electronic tunability afforded by the ability to vary the wiggler field could offer rapid frequency agility. Further, if the particle accelerator community ever returns to a desire for a high-frequency RF linac to reduce accelerator length, FELs would quite possibly be a superior source for W-band (94-GHz) concepts.

10.5 Summary

The sources in this chapter are all somewhat marginalized in the realm of HPM today, although the reasons for each depend to some degree on factors beyond the control of the device designers. Vircators are genuine workhorse sources for microwave effect testing and simulation because of their broad tunability; however, their low efficiency makes them far less attractive from the standpoint of going into the field, because of the volume and mass associated with the power and energy storage required by a low-efficiency source. In applications driven by explosive flux compression generators, though, given the energy-rich nature of this prime power source, the issue of poor efficiency may be moot. Rather, the lower characteristic impedance of these devices may make them a good electrical match to these single-shot generators. In addition, vircators are enjoying something of a renaissance today, with two new source types — the coaxial vircator and the tunable vircator — that have excited new interest and that permit new approaches to the problem of vircator efficiency.

Gyrotron development is being conducted in a very competitive international environment today, and the vitality of that environment has led to rapid advances in technology in the realms of the use and mode control of very high order azimuthal modes in cavities that are tens of free-space wavelengths in diameter; integrated quasi-optical output couplers that allow the separation of this task from beam collection; and chemical vapor deposition (CVD) artificial diamond windows to get the strength, low loss tangent, and thermal conductivity required for the high power fluxes they must transmit. Gyroklystrons have become competitors to klystrons for applications requiring a 100-MW-class amplifier in the X-band. As the frequency increases above the X-band, gyroklystrons may have a growing competitive advantage over klystrons.

Free-electron lasers offer unmatched peak power performance in the millimeter-wave region, but the number of applications requiring gigawatt millimeter-wave output from a large, complex system is extremely limited. If the particle accelerator community returned to high-frequency concepts, the FEL might be competitive for that application. At this point, though, there are no applications driving the technology in the HPM realm.

We summarize the strengths and weaknesses of the sources in this chapter in Table 10.2.

TABLE 10.2

Comparison of the Strengths and Weaknesses of the Major Source Types in This Chapter

	Strengths	Weaknesses	Notable Accomplishments
Vircators	Relatively simple generation mechanism; broadly tunable configuration; can operate without a magnetic field; low-impedance, high power operation	Low efficiency; gap closure tends to make frequency chirp during pulse	Regularly tunable over an octave, with an order of magnitude demonstrated Multigigawatt output from 1–10 GHz
Gyrotrons	High-frequency (~100 GHz) operation at MW (CW) levels with high efficiency	Immature at hundreds of MW; higher frequencies suffer significant atmospheric attenuation except near 35 and 94 GHz	1 MW at 100 to 170 GHz for long-pulse to continuous operation; 80 MW in an X-band gyroklystron
Free-electron lasers	True HPM amplifier; virtually unlimited frequency range; high power operation; high efficiency	Complicated; multimegavolt operation to achieve high frequencies; demanding beam quality requirements; higher frequencies suffer significant atmospheric attenuation except near 35 and 94 GHz	2 GW in single pulses at 140 GHz, 1-GW pulses at a repetition rate of 2 kHz for 50-pulse bursts

Problems

1. The simplest expression for microwave power produced from an electron beam of efficiency η is:

$$P = \eta VI = \eta VJA$$

The plasma in the diode gap will move across it at velocity v_p:

$$d(t) = d_0 - v_p t$$

where d_0 is the initial gap. Now, assume the temperature of the plasma is produced by ohmic heating of the plasma by the current passing through it:

$$T_\rho \sim \rho J^2$$

where ρ is the resistivity. When the plasma expands across some fraction of the gap, resonance is destroyed and microwaves cease. Therefore, microwave pulse length scales like the cathode plasma transit time across the gap

$$\tau_\mu \sim \frac{d}{v_p} \sim d\sqrt{\frac{m_p}{T_p}}$$

where T_p is the plasma temperature and m_p is the hottest light ion species, which governs the location of the conducting surface (usually hydrogen). Assume it's a Child's Law diode (Eq. 4.104). Using these relations, derive a scaling relation between microwave power and pulse length:

$$P_\mu \sim \frac{1}{\tau_\mu^{5/3}}$$

where $n = 5/3$ for a Child's Law diode.

How does pulse energy scale? From this, is there anything to be gained in energy by making longer pulses?

2. For voltages between 100 kV and 3 MV, plot I_{SCL} as a function of voltage for both solid and annular beams, with $r_0/r_b = 0.5$ and 0.8. Add the plots for an annular beam with $r_b/r_i = 0.3$ in both cases.
3. Assume a constant 5-mm standoff of the beam from the wall. Plot I_{SCL} for 1.5-MV solid and annular beams as a function of wall radius, from 1 to 5 cm.
4. A solid-cross-section beam of 30 kA and 1 MV, with a radius of 3 cm, is injected into the interaction region of a virtual cathode oscillator. What is your estimate of the virtual cathode oscillation frequency?
5. Inject a 20-kA, 500-kV beam of radius 2 cm with a solid cross section into a circular waveguide. As you increase the waveguide radius, at what waveguide radius will a virtual cathode form? At what radius is the beam current equal to $2I_{SCL}$?
6. Derive Equation 10.9.
7. Using Equation 10.10, assuming an anode–cathode gap of 2 cm, plot the expected vircator frequency as a function of diode voltage.
8. The magnetic moment for an electron in the magnetic field of a gyrotron is given in Equation 10.15:

$$\mu = \frac{\left(\frac{1}{2}mv_\perp^2\right)}{B_{0z}}$$

This quantity is an adiabatic invariant within a gyrotron if the magnetic field varies slowly enough, which we will assume to be true. The statement was made in the text that in designing a gyrotron, one must be careful not to choose too large a value of $v_\perp$, because magnetic mirroring could result. Assume that the magnetic field increases along the axis of a gyrotron from a value B_{0z1} at $z = z_1$ to a larger value B_{0z2} at $z = z_2$. Assume also that the electron has a total kinetic energy eV_0, where V_0 is the accelerating voltage in the electron gun. Let $v_{\perp 1}$ be the perpendicular velocity component at $z = z_1$. Derive an expression for the maximum value of $\alpha = v_\perp/v_z$ at $z = z_1$ in order to prevent v_z at $z = z_2$ from vanishing. Assume that the kinetic energy of an electron is conserved.

9. Plot the electron cyclotron frequency of the beam electrons as a function of accelerating voltage, neglecting space-charge depression, for a magnetic field of 1 T.
10. A gyrotron is built to a requirement that it generate 1 MW of output. If the power efficiency is increased from 33 to 50% by using a depressed collector, what is the reduction in power loss to the cavity and beam collector?
11. What magnetic field is required to achieve resonance in a gyrotron between a 300-kV electron beam and the $TE_{6,2}$ mode of a circular waveguide 3 cm in radius?
12. How much energy is stored in a magnetic field of 0.5 T that fills a cylindrical volume 5 cm in radius and 1 m long?
13. In klystron-like devices, such as a gyroklystron, when it becomes impractical to reduce the radius of the drift space between two cavities in order to cut off propagation in the lowest-order TE_{11} mode, the drift tube is sometimes lined with an absorber. If the attenuation of the absorber to this spurious mode is 5 dB/cm, and

if the spacing between cavities is 5 cm, what is the ratio of the spurious signal at the input and output of the absorbing section?

14. For a CARM using a 2-MeV electron beam, find the magnetic field required to achieve resonance at 50 GHz with a TE_{11} mode of a 3-cm-radius waveguide.
15. Redo the estimate of the frequency of an FEL, replacing the light line in Equation 10.25 with the dispersion curve for a waveguide mode. Ignore the effect of the wiggler dynamics, focusing only on the resonance between the Doppler-shifted wiggler wave and the normal mode of the waveguide. Find an expression for the FEL frequency taking account of the cutoff frequency of the waveguide mode. Find an expression also for the lower-frequency resonance with the waveguide mode.
16. A 2-MeV electron beam is injected into a circular-cross-section drift tube 4 cm in radius. What is the minimum wiggler period allowed in order to avoid backward wave interactions with the TE_{11} mode? These interactions can present a problem because the beam–backward wave interaction supports an absolute instability that can be difficult to control.
17. Consider the plot of a_w for the LLNL FEL operating at 35 GHz. Knowing the output frequency, the wiggle wavelength of $\lambda_w = 9.8$ cm, and the wiggler amplitude upstream of 0.37 T ($a_w = 2.4$), estimate the input beam energy and the energy of the spent beam after microwave generation using the data in Figure 10.44.

References

1. Benford, J., High power microwave simulator development, *Microwave J.*, 30, 97, 1987.
2. Birdsall, C.K. and Bridges, W.B., *Electron Dynamics of Diode Regions*, Academic Press, New York, 1966.
3. Sullivan, D.J., Walsh, J.E., and Coutsias, E.A., Virtual cathode oscillator (vircator) theory, in *High Power Microwave Sources*, Granatstein, V.L. and Alexeff, I., Eds., Artech House, Boston, 1987, p. 441.
4. Thode, L.E., Virtual cathode microwave device research: experiment and simulation, in *High Power Microwave Sources*, Granatstein, V.L. and Alexeff, I., Eds., Artech House, Boston, 1987, p. 507.
5. Mahaffey, R.A. et al., High-power microwaves from a non-isochronic reflexing system, *Phys. Rev. Lett.*, 39, 843, 1977.
6. Didenko, A.N. et al., The generation of high-power microwave radiation in a triode system from a heavy-current beam of microsecond duration, *Sov. Tech. Phys. Lett.*, 4, 3, 1978.
7. Brandt, H. et al., Gigawatt Microwave Emission from a Relativistic Reflex Triode, Harry Diamond Laboratory Report HDL-TR-1917, 1980.
8. Burkhart, S., Multigigawatt microwave generation by use of a virtual cathode oscillator driven by a 1–2 MV electron beam, *J. Appl. Phys.*, 62, 75, 1987.
9. Bromborsky, A. et al., On the path to a terawatt: high power microwave experiments at Aurora, *Proc. SPIE*, 873, 51, 1988.
10. Platt, R. et al., Low-frequency, multigigawatt microwave pulses generated by a virtual cathode oscillator, *Appl. Phys. Lett.*, 54, 1215, 1989.
11. Kwan, T.J.T. et al., Theoretical and experimental investigation of reditrons, *Proc. SPIE*, 873, 62, 1988.
12. Poulsen, P., Pincosy, P.A., and Morrison, J.J., Progress toward steady-state, high-efficiency vircators, *Proc. SPIE*, 1407, 172, 1991.
13. Benford, J. et al., Interaction of a vircator microwave generator with an enclosing resonant cavity, *J. Appl. Phys.*, 61, 2098, 1987.
14. Price, D., Sze, H., and Fittinghoff, D., Phase and frequency locking of a cavity vircator driven by a relativistic magnetron, *J. Appl. Phys.*, 65, 5185, 1989.
15. Fazio, M.V. et al., Virtual cathode microwave amplifier experiment, *J. Appl. Phys.*, 66, 2675, 1989.
16. Price, D., Sze, H., and Fittinghoff, D., Phase and frequency locking of a cavity vircator driven by a relativistic magnetron, *J. Appl. Phys.*, 65, 5185, 1989.
17. Sze, H., Price, D., and Harteneck, B., Phase locking of two strongly-coupled vircators, *J. Appl. Phys.*, 67, 2278, 1989.
18. Gadetskii, N.P. et al., The virtode: a generator using supercritical REB current with controlled feedback, *Plasma Phys. Rep.*, 19, 273, 1993 (*Fiz. Plazmy*, 19, 530, 1993).
19. Kitsanov, S.A. et al., S-band vircator with electron beam promodulation based on compact pulse driver with inductive energy storage, *IEEE Trans. Plasma Sci.*, 30, 1179, 2002.
20. Woolverton, K., Kristiansen, M., and Hatfield, L.L., Computer simulations of a coaxial vircator, *Proc. SPIE*, 3158, 145, 1997.
21. Jiang, W. et al., High-power microwave generation by a coaxial vircator, *Digest of Technol Papers: IEEE International Pulsed Power Conference*, Monterey, CA, 1999, p. 194.
22. Lin, T. et al., Computer simulations of virtual cathode oscillations, *J. Appl. Phys.*, 68, 2038, 1990.
23. Price, D. et al., Operational features and microwave characteristics of Vircator II, *IEEE Trans. Plasma Sci.*, 16, 177, 1988.
24. Woo, W.-Y., Two-dimensional features of virtual cathode and microwave emission, *Phys. Fluids*, 30, 239, 1987.
25. Sze, H. et al., Dynamics of a virtual cathode oscillator driven by a pinched diode, *Phys. Fluids*, 29, 3873, 1986.
26. Goldstein, S.A. et al., Focused-flow model of relativistic diodes, *Phys. Rev. Lett.*, 33, 1471, 1974.
27. Creedon, J.M., Relativistic Brillouin flow in the high v/γ diode, *J. Appl. Phys.*, 46, 2946, 1975.
28. Burkhart, S., Scarpetti, R., and Lundberg, R., Virtual cathode reflex triode for high power microwave generation, *J. Appl. Phys.*, 58, 28, 1985.
29. Davis, H.A. et al., High-power microwave generation from a virtual cathode device, *Phys. Rev. Lett.*, 55, 2293, 1985.